1-1-2020

S/N-doped carbon nanofibers affording Fe7S8 particles with superior sodium storage

Xiu Li
University of Wollongong, xl816@uowmail.edu.au

Tao Liu

Yunxiao Wang
University of Wollongong, yunxiao@uow.edu.au

Shulei Chou
University of Wollongong, shulei@uow.edu.au

Xun Xu
University of Wollongong, xun@uow.edu.au

See next page for additional authors

S/N-doped carbon nanofibers affording Fe7S8 particles with superior sodium storage

Abstract

2020 Iron sulfides draw much attention as electrode candidates for sodium-ion batteries (SIBs) due to the rich chemical stoichiometries and high capacity. However, they usually exhibit poor cycling performance due to the large volume change during sodiation/desodiation process. In this work, we embed Fe7S8 nanoparticles into sulfur, nitrogen-doped carbon (S/N-C) nanofibers through electrospinning/sulfurization processes. The heteroatom doped carbon matrixes could effectively protect the Fe7S8 from structural collapse, obtaining a stable cycling performance. Moreover, the conductive matrixes with 1D structure can facilitate the diffusion of electrons, leading to good rate capability. As results, the as-designed Fe7S8@S/N-C nanofibers present a discharge capacity of 347 m Ah g−1 after 150 cycles at 1 A g−1 and a high rate capacity of 220 m Ah g−1 at 5 A g−1 in virtue of unique structural characteristics.

Keywords

superior, particles, carbon, fe7s8, s/n-doped, affording, nanofibers, storage, sodium

Disciplines

Engineering | Physical Sciences and Mathematics

Publication Details

Li, X., Liu, T., Wang, Y., Chou, S., Xu, X., Cao, A. & Chen, L. (2020). S/N-doped carbon nanofibers affording Fe7S8 particles with superior sodium storage. Journal of Power Sources, 451

Authors

Xiu Li, Tao Liu, Yunxiao Wang, Shulei Chou, Xun Xu, Anmin Cao, and Libao Chen

S/N-doped Carbon Nanofibers Affording Fe_7S_8 Particles with Superior Sodium Storage

Xiu Li,[a, b] Tao Liu,[c] Yun-Xiao Wang,[a] Shu-Lei Chou,[a] Xun Xu,[a,] Anmin Cao[b] and Libao Chen[c,*]*

[a]*Institute for Superconducting and Electronic Materials, University of Wollongong, Wollongong, NSW 2500, Australia.*

[b]*Key Laboratory of Molecular Nanostructure and Nanotechnology and Beijing National Laboratory for Molecular Sciences, Institute of Chemistry, Chinese Academy of Sciences (CAS), Beijing 100190, P. R. China*

[c]*State Key Laboratory of Powder Metallurgy, Central South University, Changsha, Hunan 410083, P. R. China*

Corresponding authors: Xun Xu and Libao Chen

Email: xun@uow.edu.au (Dr. X. Xu); lbchen@csu.edu.cn (Prof. L. Chen)

Abstract Iron sulfides draw much attention as electrode candidates for sodium-ion batteries (SIBs) due to the rich chemical stoichiometries and high capacity. However, they usually exhibit poor cycling performance due to the large volume change during sodiation/desodiation process. In this work, we embed Fe_7S_8 nanoparticles into sulfur, nitrogen-doped carbon (S/N-C) nanofibers through electrospinning/sulfurization processes. The heteroatom doped carbon matrixes could effectively protect the Fe_7S_8 from structural collapse, obtaining a stable cycling performance. Moreover, the conductive matrixes with 1D structure can facilitate the diffusion of electrons, leading to good rate capability. As results, the as-designed Fe_7S_8@S/N-C nanofibers present a discharge capacity of 347 m Ah g^{-1} after 150 cycles at 1 A g^{-1} and a high rate capacity of 220 m Ah g^{-1} at 5 A g^{-1} in virtue of unique structural characteristics.

Keywords: Fe_7S_8; Carbon nanofibers; Anode; Sodium-ion batteries; S, N-co-doping

1. Introduction

Lithium ion batteries (LIBs) have been commercially applied into portable devices for several decades.[1-2] With the merging of electric vehicles and large-scaled energy storage systems, however, the concerns of limited lithium resources and high prices forced researchers to explore alternative batteries systems with low-cost and high energy density. Considering these, sodium ion batteries (SIBs) have drawn great attention due to the nature abundance of sodium resources in earth and the similar electrochemical mechanism to LIBs.[3-7] However, the real practical application of SIBs is hampered by the anode materials, which always showed low specific capacity and poor cycling stability.[8-11] Therefore, exploring suitable anode materials for SIBs with advanced electrochemical performance is essential for further development of SIBs. Among the reported anode materials, iron sulfides have drawn much attention due to their relatively high specific capacity, abundant resources and low-cost.[12-23] However, Nevertheless, iron sulfides usually suffer poor electrochemical performance due to the intrinsic sluggish kinetics, poor conductivity and severe volume change during sodiation process, which affect the rate capability and cycling stability and prevent their potential application as anode materials for SIBs.

To overcome these drawbacks, preparing nanostructured iron sulfides combined with conductive matrixes is a promising strategy.[24-31] On the one hand, nano-sized materials usually could short the diffusion length of ions and electrons, resulting in fast reaction kinetics and good rate capability. In addition, nanostructured materials can alleviate

mechanical stress and maintain the integrity of materials without fractures, leading to good cycling stability. On the other hand, conductive matrixes can improve the conductivity of electrode materials, enhancing the utilization of iron sulfides and resulting in high capacity. Moreover, the conductive matrixes also could alleviate the volume changes of iron sulfides during cycling, obtaining long stable cycling performance. Therefore, preparing nanostructured iron sulfides combined with conductive matrixes materials as anode materials for SIBs could obtain good cycling stability and excellent rate capability.

Herein, we embedded Fe_7S_8 nanoparticles into sulfur and nitrogen doped carbon nanofibers (S/N-C) through electrospinning method. The whole experimental process was shown in **Scheme 1**. First, the α-Fe_2O_3 nanoparticles were synthesized *via* hydrothermal method, then the prepared α-Fe_2O_3 nanoparticles and polyacrylonitrile (PAN) was added into N,N-dimethylformamide (DMF) for electrospinning. The Fe_7S_8@S/N-C were obtained after annealing α-Fe_2O_3@PAN composites with sulfur at high temperature. The heteroatoms doped carbon nanofibers as conductive matrixes could alleviate the volume expansion Fe_7S_8 nanoparticles, avoid the agglomeration, and maintain the structure stability of electrode materials, resulting in stable cycling stability. In addition, the heteroatom could further improve the electronic conductivity of carbon nanofibers and provides more active sites for sodium storage. And the isolated Fe_7S_8 nanoparticles can display high specific capacity. Owing to unique structural characteristics, the Fe_7S_8@S/N-C electrodes exhibited stable cycling performance with a discharge capacity of 347 mA h g^{-1} after 150 cycles at 1 A g^{-1} and superior rate

capability showing a capacity of 220 mA h g^{-1} at 5 A g^{-1}.

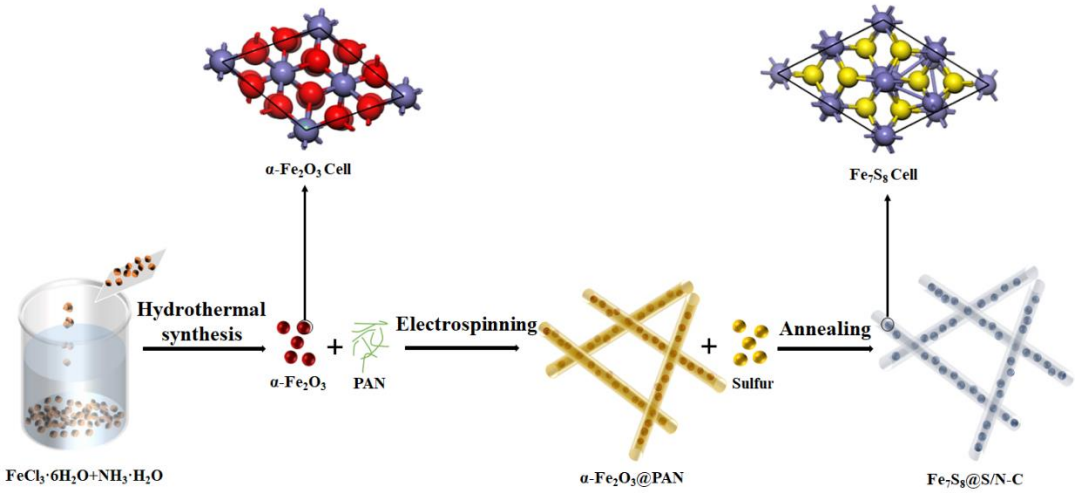

Scheme 1. Illustrative synthesis scheme of Fe_7S_8@S/N-C nanofibers.

2. Experimental section

2.1 Synthesis of Fe_7S_8@S/N-C

α-Fe_2O_3 nanoparticles were prepared through a simple hydrothermal method according to the literature with minor modification.[32] In a typical synthesis, 0.54 g $FeCl_3 \cdot 6H_2O$ was firstly dissolved into 20 mL deionized water. Then, 10 mL aqueous ammonia was added drop by drop. After that, this mixture was transferred into an autoclave and maintained at 180 °C for 12 h. The resulting product was collected by centrifugation and washed with DI water and ethanol several times.

The Fe_7S_8@S/N-C composites were synthesized through the electrospinning/sulfidation processes. Typically, 0.5 g as-prepared α-Fe_2O_3

nanoparticles and 1 g polyacrylonitrile (PAN) were added into 10 mL N,N-dimethylformamide (DMF), which were stirred at 60 °C for overnight to form a stable suspension. Then, the obtained suspension was transferred into a syringe. A stainless-steel plate was placed to collect the nanofibers with 15 cm away from the syringe. The flow rate was about 0.4 mL h^{-1} and the voltage was applied to 15 kV. The collected nanofibers were pre-oxidized at 230 °C for 2 h in air. At last, the pre-treated nanofibers were sulfureted with sulfur at 600 °C for 2 in argon atmosphere to obtain Fe_7S_8@S/N-C. For comparison, 0.5 g α-Fe_2O_3 nanoparticles and 0.5 g sulfur power were heated under the same condition to transfer α-Fe_2O_3 to Fe_7S_8. The pure S/N-C nanofibers were synthesized by the same electrospinning method without adding α-Fe_2O_3 precursor.

2.2 Materials characterization

The morphologies information of the prepared samples were characterized by the scanning electron microscope (SEM, Hitachi S4800) with Energy Dispersive Spectrometer (EDS) and field-emission transmission electron microscope (TEM, Tecnai G2 20). The X-ray diffractions (XRD, Rigaku D/max-2500 X-ray diffractometer, Cu Kα, λ = 0.154056 nm) were carried out with a scan rate of 8° min^{-1}. The thermogravimetric analysis (TGA) was conducted in air using the STD Q600 thermogravimetric analyzer. The Brunauer-Emmett-Teller (BET) surface area and pore size distribution were obtained by a Nova 2000e volumetric adsorption analyzer. Raman spectra were carried out using a HORIBA LabRAM HR Evolution Raman spectrometer. The X-ray photoelectron spectroscopies (XPS) was characterized to

evaluate the elemental composition of the samples on a Thermo scientific K_α spectrometer.

2.3 Electrochemical measurements

For the electrochemical evaluations, the working electrodes were prepared by combining 80 wt% active materials, 10 wt% acetylene black and 10 wt% carboxymethyl cellulose (CMC), which were dissolved into water and stirred for overnight to form a slurry. Then, the slurry was pasted on the Cu foil to get the electrodes. The specific capacity was calculated based on the whole mass of the electrode. A sodium foil was used as the counter electrode. The used electrolyte was 1 M $NaClO_4$ in the propylene carbonate and ethylene carbonate (EC-PC, 1:1, v:v), and glass fiber (Whatman, Grade GF/A) was utilized as the separator. The CR2025-type coin cells were assembled in the Ar-filled glove box. Galvanostatic charge-discharge test were measured at room temperature with the voltage range of 0.01 - 2.5 V.

3. Results and Discussion

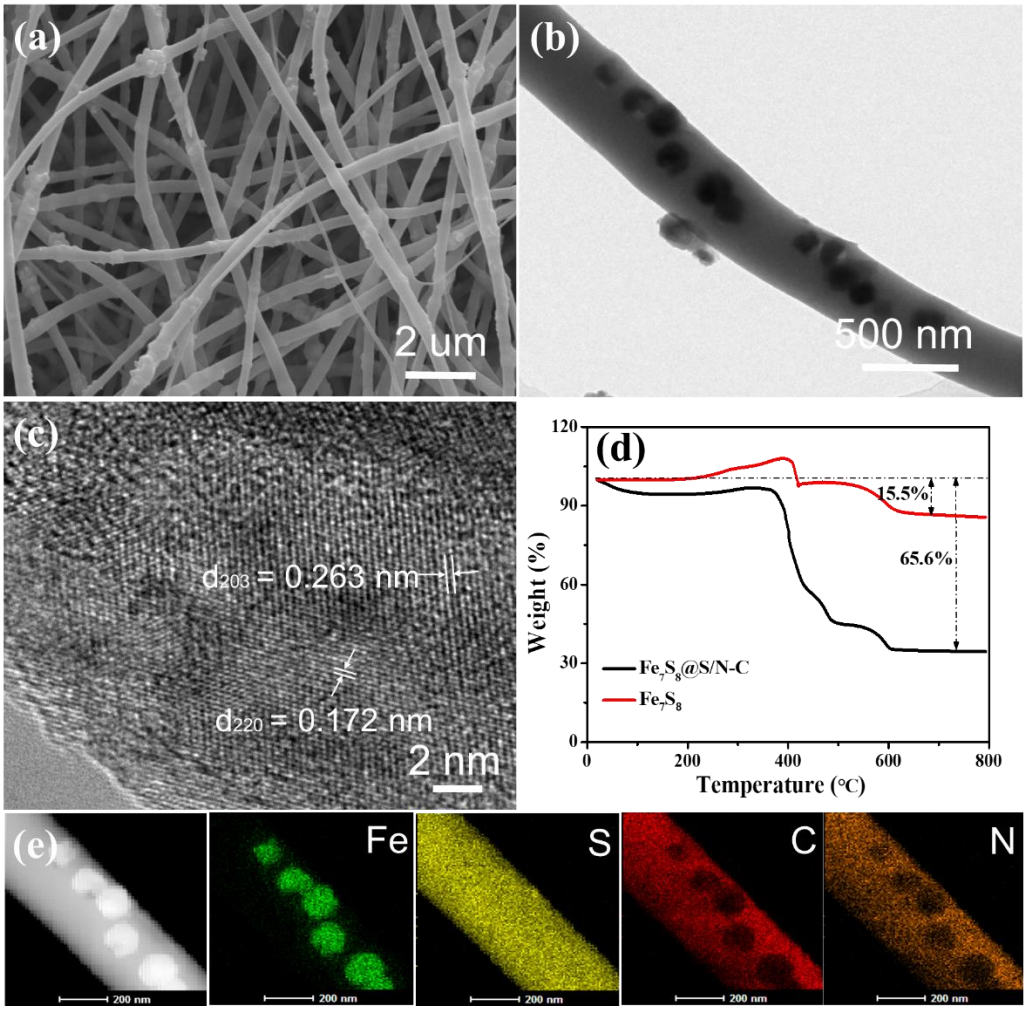

Figure 1 (a) SEM image of Fe_7S_8@S/N-C nanofibers; (b) Low-resolution and (c) high-resolution TEM images of Fe_7S_8@S/N-C nanofibers; (d) TGA curves of prepared Fe_7S_8 nanoparticles and Fe_7S_8@S/N-C nanofibers in air atmosphere; (e) Element mapping of Fe_7S_8@S/N-C nanofibers.

The morphologies and structures of prepared α-Fe_2O_3, Fe_7S_8, Fe_7S_8@S/N-C and S/N-C samples were characterized by SEM and TEM techniques, which were shown in **Figure 1** and **Figure S1**. As shown in Figure S1 a, the prepared α-Fe_2O_3 particles with size about 150 nm show a uniform morphology, which make it possible to be electrospun into PAN polymer fibers. After sulfureted process, α-Fe_2O_3 particles were successfully transferred into Fe_7S_8 particles (Figure S1 b), which exhibited irregular particle morphology with agglomeration and had a diameter of 100 - 400 nm. The HR-TEM

image of Fe_7S_8 particles show clear lattice fringes, indicating the crystal structure of obtained Fe_7S_8 materials (Figure S1 c). The designed Fe_7S_8@S/N-C samples show fiber-like structure and there are no particles on the surface, as shown in **Figure 1a**, which confirms that the Fe_7S_8 particles were embedded into carbon nanofibers. The TEM images further show the Fe_7S_8 particles were isolated distributed in the carbon matrixes (**Figure 1b)**. The HR-TEM image of Fe_7S_8@S/N-C in **Figure 1c** indicates that two lattice fringes with 0.263 nm and 0.172 nm can be observed, which are assigned to the (203) and (220) planes, respectively. The morphology of S/N-C nanofibers without Fe_7S_8 was also characterized by SEM and HR-TEM images (Figure S1 d), which indicated the uniform size distribution and amorphous structure of S/N-C nanofibers. The content Fe_7S_8 in the Fe_7S_8@S/N-C composites was measured using the thermogravimetric analysis (TGA), which was carried out in air atmosphere, as shown in **Figure 1d**. For Fe_7S_8, there is an obvious mass increasing below 400 °C due to the oxidation of Fe^{2+} to Fe^{3+}. In the range of 400 - 600 °C, the Fe_7S_8 particles was completely transferred into Fe_2O_3, causing the weight loss of 15.5%. For the Fe_7S_8@S/N-C composite, there are two stage weight loss: the first one between 380 - 480 °C is related to the consumption of carbon; the second one between 480 - 600 °C was ascribed to the transformation of Fe_7S_8 into Fe_2O_3. It can be calculated that the content of Fe_7S_8 in Fe_7S_8@S/N-C composite was ~ 39.8 %. The energy dispersive X-ray (EDX) element mapping images indicated that the S, C, and N elements are uniformly distributed throughout the Fe_7S_8@S/N-C nanofiber (**Figure 1e**), while Fe element is isolated distributed due to the distribution of isolated Fe_7S_8 nanoparticles in

the nanofibers, which is consistent with the results of TEM images.

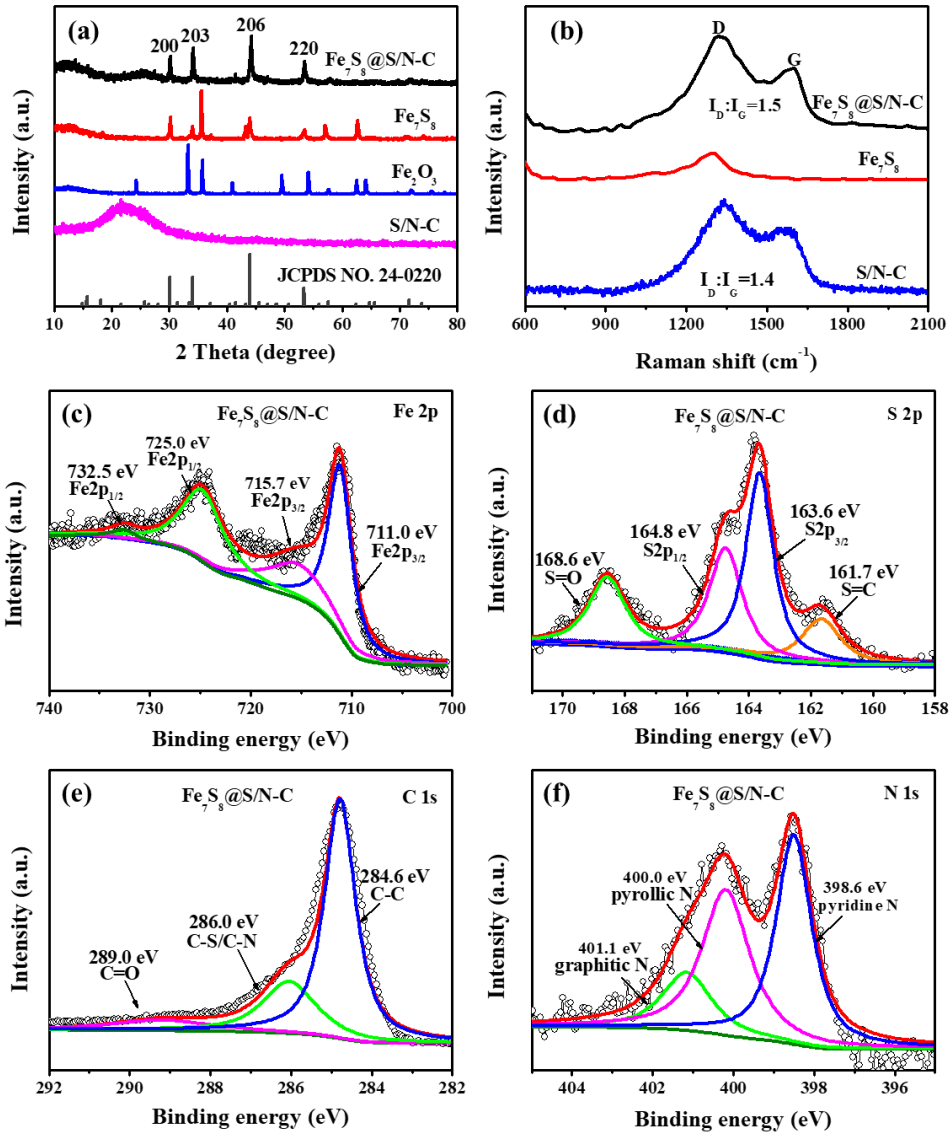

Figure 2 (a) XRD patterns of as-prepared α-Fe_2O_3, Fe_7S_8, S/N-C and Fe_7S_8@S/N-C samples; (b) Raman spectra of as-prepared Fe_7S_8, S/N-C and Fe_7S_8@S/N-C samples; High-resolution XPS spectra of Fe_7S_8@S/N-C: (c) Fe 2p; (d) S 2p; (e) C 1s; (f) N 1s.

XRD measurement was carried out to characterize the crystal phase of as-prepared α-Fe_2O_3, Fe_7S_8, Fe_7S_8@S/N-C and S/N-C samples, as shown in **Figure 2a**. The all diffraction patterns of Fe_7S_8, Fe_7S_8@S/N-C can be well indexed to pyrrhotite Fe_7S_8 (JCPDS No. 24-0220), indicating that the α-Fe_2O_3 particles were completely

transformed into Fe_7S_8 materials. Moreover, there are no other impurity peaks, suggesting the good crystallinity and high purity. The XRD pattern of S/N-C is ascribed to the typical carbon. As displayed in Raman spectra (**Figure 1b**), Fe_7S_8@S/N-C and S/N-C samples show D peak (1320 cm^{-1}) and G peak (1590 cm^{-1}). The intensity ratio of the D peak to G peak for Fe_7S_8@S/N-C (I_D : I_G, 1.5) and S/N-C samples (I_D : I_G, 1.4) indicates that there are more defect sites in Fe_7S_8@S/N-C, which might be caused by the N and S more doping.[33] The Raman spectrum of pure Fe_7S_8 only shows some small peaks located at ~ 1390 cm^{-1}, which are attribute to the small defect site in Fe_7S_8.[34]

To understand the chemical status of Fe_7S_8@S/N-C, XPS measurement was conducted. The Fe 2p spectrum in **Figure 2c** shows two valences of Fe existed in the sample. The peaks of Fe $2p_{3/2}$ located at 711 eV and 715.7 eV (satellite peak) indicate the existence of Fe^{2+}, while the Fe $2p_{1/2}$ peaks at 725 eV and 732.5 eV (satellite peak) can be assigned to Fe^{3+}.[35] In the S 2p spectrum (**Figure 2d**), the peaks at 163.6 eV and 164.8 eV can be attributed to the S^{2-} and S_n^{2-}.[36] The small peak at 161.7 eV suggests that some C-S bonds formed during sulfidation process. Besides, another peak located at 168.6 eV can be indexed to the S-O bond caused by the adsorbed oxygen on the active surface of Fe_7S_8 particles in the sample.[37] In C 1s spectrum (**Figure 2e**), the peaks at 289.0, 286 and 284.6 eV are attributed to C=O, C-N/C-S and C-C bonding, respectively. In addition, N 1s spectrum in **Figure 2f** reveals the existing of pyridine, pyrrolic and graphitic N.[38] In this work, the S/N-C matrixes could provides many advantages for improving the electrochemical performance of Fe_7S_8@S/N-C composites. First, the N and S atoms can enhance the electronic conductivity of the composites. Second, the defect sites

brought by N and S could offer much more absorption site for Na ions to improve its capacitive capability. Third, the 1D disorder honeycomb carbon could offer short diffusion length for Na^+, resulting in good rate performance. The N_2 adsorption-desorption isotherms of Fe_7S_8@S/N-C, S/N-C and Fe_7S_8 samples was also shown in **Figure S2**. The Brunauer-Emmett-Teller (BET) of the Fe_7S_8@S/N-C composites (21.41 g m^{-2}) show higher specific surface area than that of S/N-C (14.47 g m^{-2}) and Fe_7S_8 (14.47 g m^{-2}), which provides more active site for Na^+ adsorption.

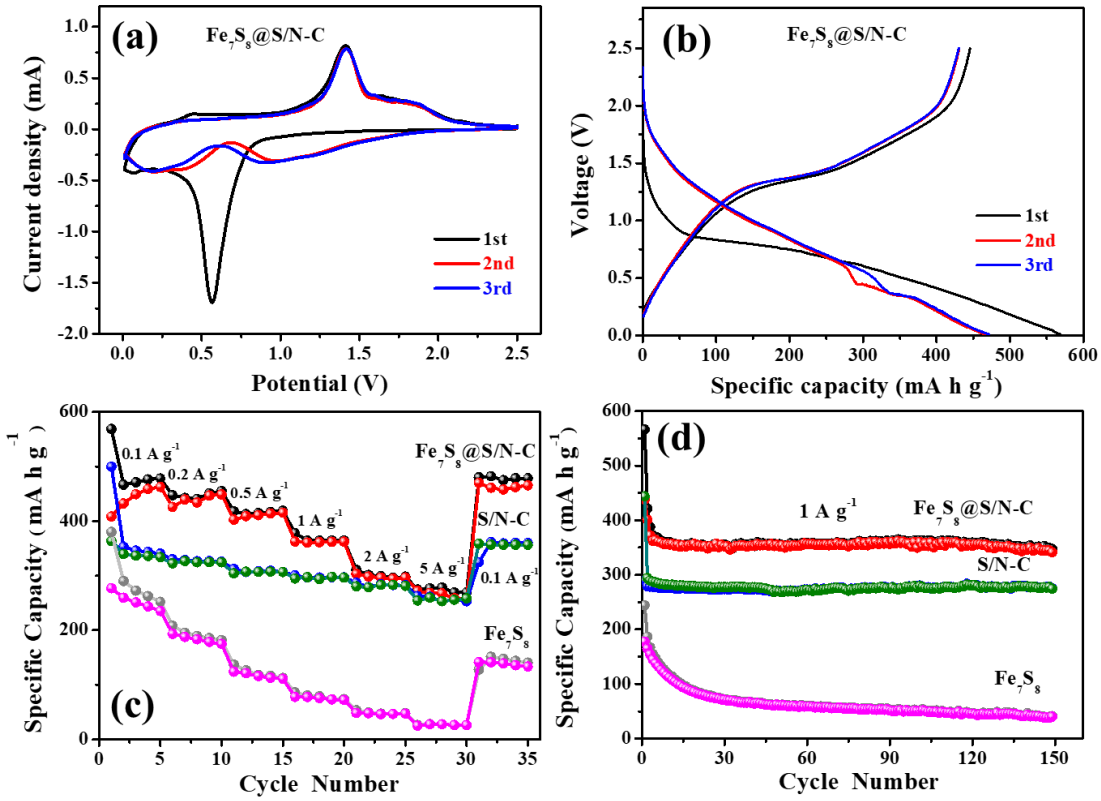

Figure 3 (a) CV curves at 0.2 mV s^{-1} and (b) charge-discharge profiles at 0.1 A g^{-1} of the Fe_7S_8@S/N-C electrode. (c) Rate capability of Fe_7S_8@S/N-C, Fe_7S_8 and S/N-C electrodes at various current densities. (d) Cycling performance of Fe_7S_8@S/N-C, Fe_7S_8 and S/N-C electrodes at 1 A g^{-1}.

The Na storage performance of the Fe_7S_8@S/N-C, Fe_7S_8 and S/N-C electrodes was evaluated, which are shown in **Figure 3**. **Figure 3a** exhibits the initial three CV scans

of Fe_7S_8@S/N-C electrode. During the first scan process, there exists a sharp cathodic peak at ~0.6 V, presenting the intercalation reaction (***Eqn.* 1**) and the formation of electrolyte interphase (SEI) film. In the low potential range, the small cathodic peak is ascribed to the conversion reaction to form Fe and Na_2S (***Eqn.* 2**).[21] In the first anodic scan, the sharp peak at 1.4 V and broad peak at about 1.6-2.0 V indicate the counter reaction of conversion reaction (***Eqn.* 3**) and the deintercalation reaction (***Eqn.* 4**), respectively.[18] According previous work, only part of Na ions can be deintercalated out of the Fe_7S_8-based electrode, leading to the irreversible capacity of the initial cycle.

Sodiation: $Fe_7S_8 + 8Na^+ + 8e^- \rightarrow 4Na_2FeS_2 + 3Fe$ (1)

$Na_2FeS_2 + 2Na^+ + 2e^- \rightarrow 2Na_2S + Fe$ (2)

Desodiation: $2Na_2S + Fe \rightarrow Na_2FeS_2 + 2Na^+ + 2e^-$ (3)

$Na_2FeS_2 \rightarrow Na_{2-x}FeS_2 + xNa^+ + xe^-$ (4)

In the subsequent cathodic scans, the sharp peak at 0.6 V became broader and shifted to 0.95 V because of the formation of SEI film. Besides, the CV profiles of the 2nd and 3rd cycles did not change obviously, demonstrating a good structural stability. For Fe_7S_8 electrode, as shown in **Figure S3 a**, it suffered a worse reversibility. During the second and third cycles, the intercalation reaction of Na^+ ion could hardly take place, indicating the S,N-doped carbon nanofibers could effectively protect the Fe_7S_8 from structure collapse and improving its cycling reversibility. In **Figure S3 b**, the CV profiles of S/N-C electrode shows a reduction peak around at 0.5 V in the first cycle, which is ascribed

to the formation of an irreversible solid electrolyte interphase (SEI) film. In the following cycles, the curves are well overlapped, demonstrating good reversibility.

The charge-discharge profiles of the first three cycles for the Fe_7S_8@S/N-C was displayed in **Figure 3b**. During the first discharge process, a remarkable plateau located at 0.9 - 0.6 V was attributed to the irreversible intercalation reaction and formation of SEI film. In the subsequent cycles, two plateaus can be observed, caused by the reversible intercalation and conversion reactions. In contrast, for Fe_7S_8 and S/N-C electrodes (**Figure S3 c** and **d**), there was no remarkable plateau on the discharge profiles during the 2nd and 3rd cycles. Moreover, the coincidence of subsequent discharge/charge curves for Fe_7S_8@S/N-C and S/N-C electrodes indicates that S/N-C could afford Fe_7S_8 with a reversible and stable Na storage performance. Benefited from the defect-decorated carbon nanofibers as conductive matrix with high ion diffusion rate, the Fe_7S_8@S/N-C electrode showed the best rate capability among three electrodes, as shown in **Figure 3c**. With the current density increasing, the Fe_7S_8@S/N-C electrode delivered capacities of 470, 445, 415, 365, 280 and 220 mA h g^{-1}, at 0.1, 0.2, 0.5, 1, 2, 5 A g^{-1}, respectively. When the current density was adjusted back to 0.1 A g^{-1}, a capacity of 475 mA h g^{-1} could still be obtained. The Fe_7S_8 electrode only showed the limited capacities of 272, 208, 137, 86, 53 and 26 mA h g^{-1}, at current densities of 0.1, 0.2, 0.5, 1, 2, 5 A g^{-1}, respectively. Besides, when current density was back to 0.1 A g^{-1}, Fe_7S_8 electrode only offered a capacity of 147 mA h g^{-1}. This suggests that S/N-C nanofibers could improve the performance of Fe_7S_8 in the stability and conductivity. Moreover, although S/N-C also exhibited good stability and rate capability, it sustained relatively

lower capacities than Fe_7S_8@S/N-C at all current densities. As shown in **Figure 3d**, Fe_7S_8@S/N-C still showed a high capacity of 347 mA h g^{-1} after 150 cycles at 1 A g^{-1}, with the retention rate of about 94% (compared with the 2nd cycle). However, the Fe_7S_8 and S/N-C displayed a capacity of 41 and 274 mA h g^{-1} at the same current density after 150 cycles, respectively. The better rate and cycling performance of Fe_7S_8@S/N-C composites could be ascribed to the following reasons: first, the carbon matrixes can alleviate the volume change of Fe_7S_8 particles during sodiation/desodiation process, maintaining the structure stability. Moreover, the 1D matrixes offer short Na^+ diffusion length, leading to good rate capability. Second, the heteroatom could further improve the conductivity of the prepared sample, benefitting the transportation of electrons, which can be proved by the EIS profiles. The EIS profiles of the Fe_7S_8@S/N-C and Fe_7S_8 electrodes are show in **Figure S4**. Before and after galvanostatic tests, the charge transfer resistances of Fe_7S_8@S/N-C were both smaller than those of Fe_7S_8, indicating the higher electronic conductivity of Fe_7S_8@S/N-C.

To explore the sodium storage kinetics of Fe_7S_8@S/N-C electrode, CV measurements were carried out at various scan rate from 0.2 to 5 mV s^{-1}. As shown in **Figure 4a**, both the anodic and cathodic peaks became broader with the increasing of scan rate. The curves at low and high scan rates show the similar shapes, indicating a small polarization voltage. It is reported that the electrochemical energy storage for metal sulfides is generally consisted of two parts: diffusion-controlled process and capacitance-controlled behavior. The relationship between the peak current (i) and sweep rate (v) obey the law, as following:[39]

$$i = av^b \qquad (5)$$

where a and b are adjustable parameters. When the b-value closes to 0.5, it indicates the diffusion-controlled process. While the b-value closes to 1, it indicates the capacitance-controlled behavior. The b-value can be calculated by fitting the log(v) to log(i). Surprisingly, depending on the calculation result, the b-values are 0.88, and 0.68 for anodic and cathodic peaks, respectively, as shown in **Figure 4b**.

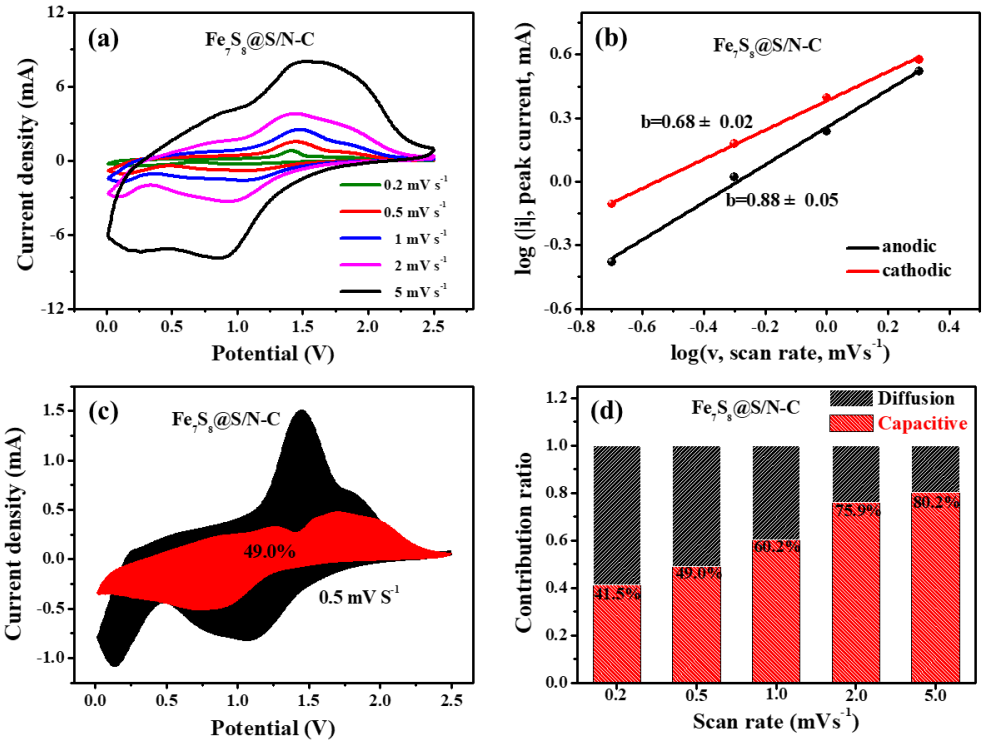

Figure 4 (a) CV curves at various sweep rates from 0.2 to 5 mV s^{-1}; (b) relationship between the peak currents and scan rates in logarithmic format; (c) capacitive contribution at a scan rate of 0.5 mV s^{-1} and (d) contribution ratio of the capacitive and diffusion-controlled capacity of Fe_7S_8@S/N-C electrode.

The total capacitive contribution to the total capacity can be calculated by the following equations:[40]

$$i = k_1 v + k_2 v^{1/2} \quad (6)$$

where $k_1 v$ reveals the capacitive contribution and $k_2 v$ represents the diffusion-controlled contribution. As shown in **Figure 4c**, 49.0% of the total capacity at the scan rate of 0.5 mV s^{-1} was contributed from capacitive controlled processes for Fe_7S_8@S/N-C electrode. From **Figure 4d**, the contribution ratio of capacitance-controlled process gradually increased with the increasing of the scan rates and finally a maximum value of 80.2% achieved at 5 mV s^{-1}. For pure Fe_7S_8 electrode, based on the calculation of CV curves (**Figure S5 a**), a high ratio of capacitive contribution at various scan rate was also obtained, as shown in **Figure S5 b**. It indicates that the fast charge-discharge process not only occurs on the defect-site of S, N-doped carbon nanofibers, but also takes place on the surface of Fe_7S_8.

4. Conclusions

In summary, we have successfully synthesized the Fe_7S_8@S/N-C nanofibers by electrospinning/sulfidation methods. The S/N-C nanofibers matrixes could offer this composite good structure stability by preventing the collapse of Fe_7S_8 during charge/discharge process. Moreover, the stable 1D structure facilitate the transportation of ions and electrons, leading to good rate capability. And Fe_7S_8 nanoparticles grantee a high specific capacity. As results, the Fe_7S_8@S/N-C demonstrated superior rate capability (a specific capacity of 220 mA h g^{-1} at 5 A g^{-1}) and stable cycling performance (a specific capacity of 347 mA h g^{-1} at 1 A g^{-1} after 150 cycles). This work will give useful guidance to design other metal sulfide anodes with the adjustment of structure

and compositions.

Acknowledgments

This work was financially supported by an Australian Research Council (ARC) Linkage Project (DP160102627 and DE170100928).

References

(1) Wang, L.; Xie, X.; Dinh, K. N.; Yan, Q. Y.; Ma, J. M. Synthesis, Characterizations, and Utilization of Oxygen-Deficient Metal Oxides for Lithium/Sodium-Ion Batteries and Supercapacitors. *Coord. Chem. Rev.* **2019,** *397*, 138-167.
(2) Wu, D.; Wang, C.; Wu, M.; Chao, Y.; He, P.; Ma, J. Porous Bowl-Shaped VS_2 Nanosheets/Graphene Composite for High-Rate Lithium-Ion Storage. *J. Eenergy Chem.* **2020,** *43*, 24-32.
(3) Lu, P.; Sun, Y.; Xiang, H. F.; Liang, X.; Yu, Y. 3D Amorphous Carbon with Controlled Porous and Disordered Structures as a High-Rate Anode Material for Sodium-Ion Batteries. *Adv. Energy Mater.* **2018,** *8*, 1702434.
(4) Hou, H. S.; Qiu, X. Q.; Wei, W. F.; Zhang, Y.; Ji, X. B. Carbon Anode Materials for Advanced Sodium-Ion Batteries. *Adv. Energy Mater.* **2017,** *7*, 1602898.
(5) Xu, J. T.; Wang, M.; Wickramaratne, N. P.; Jaroniec, M.; Dou, S. X.; Dai, L. M. High-Performance Sodium Ion Batteries Based on a 3D Anode from Nitrogen-Doped Graphene Foams. *Adv. Mater.* **2015,** *27*, 2042-2048.
(6) Sun, Y.; Guo, S. H.; Zhou, H. S. Exploration of Advanced Electrode Materials for Rechargeable Sodium-Ion Batteries. *Adv. Energy Mater.* **2019,** *9*, 1800212.
(7) Huang, Y. X.; Zhao, L. Z.; Li, L.; Xie, M.; Wu, F.; Chen, R. J. Electrolytes and Electrolyte/Electrode Interfaces in Sodium-Ion Batteries: From Scientific Research to Practical Application. *Adv. Mater.* **2019,** *31*, 1808393.
(8) Wang, Q.; Zhao, C.; Lu, Y.; Li, Y.; Zheng, Y.; Qi, Y.; Rong, X.; Jiang, L.; Qi, X.; Shao, Y. Advanced Nanostructured Anode Materials for Sodium-Ion Batteries. *Small* **2017,** *13*, 1701835.
(9) Kim, Y.; Ha, K. H.; Oh, S. M.; Lee, K. T. High-Capacity Anode Materials for Sodium-Ion Batteries. *Chem.-Eur. J.* **2014,** *20*, 11980-11992.
(10) Balogun, M.-S.; Luo, Y.; Qiu, W.; Liu, P.; Tong, Y. A Review of Carbon Materials and Their Composites with Alloy Metals for Sodium Ion Battery Anodes. *Carbon* **2016,** *98*, 162-178.
(11) Xie, F.; Zhang, L.; Ye, C.; Jaroniec, M.; Qiao, S. Z. The Application of Hollow Structured Anodes for Sodium-Ion Batteries: From Simple to Complex Systems. *Adv. Mater.* **2019,** *31*, 1800492.
(12) Wei, X.; Li, W. H.; Shi, J. A.; Gu, L.; Yu, Y. FeS@C on Carbon Cloth as Flexible

Electrode for Both Lithium and Sodium Storage. *ACS Appl. Mater. Interfaces* **2015,** *7*, 27804-27809.
(13) Li, D. H.; Sun, Y. Y.; Chen, S.; Yao, J. Y.; Zhang, Y. H.; Xia, Y. Z.; Yang, D. J. Highly Porous FeS/Carbon Fibers Derived from Fe-Carrageenan Biomass: High-Capacity and Durable Anodes for Sodium-Ion Batteries. *ACS Appl. Mater. Interfaces* **2018,** *10*, 17175-17182.
(14) Wang, Q. H.; Zhang, W. C.; Guo, C.; Liu, Y. J.; Wang, C.; Guo, Z. P. In Situ Construction of 3D Interconnected FeS@Fe_3C@ Graphitic Carbon Networks for High-Performance Sodium-Ion Batteries. *Adv. Funct. Mater.* **2017,** *27*, 1703390.
(15) Lee, S. Y.; Kang, Y. C. Sodium-Ion Storage Properties of FeS-Reduced Graphene Oxide Composite Powder with a Crumpled Structure. *Chem.-Eur. J.* **2016,** *22*, 2769-2774.
(16) Jin, A.; Kim, M. J.; Lee, K. S.; Yu, S. H.; Sung, Y. E. Spindle-Like Fe_7S_8/N-Doped Carbon Nanohybrids for High-Performance Sodium Ion Battery Anodes. *Nano Res.* **2019,** *12*, 695-700.
(17) Liu, Z. M.; Hu, F.; Xiang, J.; Yue, C.; Lee, D.; Song, T. A Nano-Micro Hybrid Structure Composed of Fe_7S_8 Nanoparticles Embedded in Nitrogen-Doped Porous Carbon Framework for High-Performance Lithium/Sodium-Ion Batteries. *Part. Part. Syst. Char.* **2018,** *35*, 1800163.
(18) Chen, W. H.; Zhang, X. X.; Mi, L. W.; Liu, C. T.; Zhang, J. M.; Cui, S. Z.; Feng, X. M.; Cao, Y. L.; Shen, C. Y. High-Performance Flexible Freestanding Anode with Hierarchical 3D Carbon-Networks/Fe_7S_8/Graphene for Applicable Sodium-Ion Batteries. *Adv. Mater.* **2019,** *31*, 1806664.
(19) Choi, M. J.; Kim, J.; Yoo, J. K.; Yim, S.; Jeon, J.; Jung, Y. S. Extremely Small Pyrrhotite Fe_7S_8 Nanocrystals with Simultaneous Carbon-Encapsulation for High-Performance Na-Ion Batteries. *Small* **2018,** *14*, 1702816.
(20) Zhang Q.; Liao J.; Liao M.; Dai J. Y; Ge H. L.; Duan T.; Yao W. T. One-dimensional Fe_7S_8@C nanorods as anode materials for high-rate and long-life lithium-ion batteries. *Appl. Surf. Sci.*, 2019, *473*, 799-806.
(21) Shi, L. D.; Li, D. Z.; Yu, J. L.; Liu, H. C.; Zhao, Y.; Xin, H. L.; Lin, Y. M.; Lin, C. D.; Li, C. H.; Zhu, C. Z. Uniform Core-Shell Nanobiscuits of Fe_7S_8@C for Lithium-Ion and Sodium-Ion Batteries with Excellent Performance. *J. Mater. Chem. A* **2018,** *6*, 7967-7976.
(22) Li, Q. D.; Wei, Q. L.; Zuo, W. B.; Huang, L.; Luo, W.; An, Q. Y.; Pelenovich, V. O.; Mai, L. Q.; Zhang, Q. J. Greigite Fe_3S_4 as a New Anode Material for High-Performance Sodium-Ion Batteries. *Chem. Sci.* **2017,** *8*, 160-164.
(23) Liu, Q. S.; Gao, J. L.; Cao, C. T.; Yin, G. P.; Jiang, Z. X.; Ge, M. Y.; Xiao, X. H.; Lee, W. K.; Wang, J. J. Insights into Enhanced Sodium Ion Storage Mechanism in Fe_3S_4: The Coupling of Surface Chemistry, Microstructural Regulation and 3d Electronic Transport. *Nano Energy* **2019,** *62*, 384-392.
(24) Chen, W.; Zhang, X.; Mi, L.; Liu, C.; Zhang, J.; Cui, S.; Feng, X.; Cao, Y.; Shen, C. High-Performance Flexible Freestanding Anode with Hierarchical 3D Carbon-Networks/Fe_7S_8/Graphene for Applicable Sodium-Ion Batteries. *Adv. Mater.* **2019,** *31*, 1806664.

(25) Huang, S.; Fan, S.; Xie, L.; Wu, Q.; Kong, D.; Wang, Y.; Von Lim, Y.; Ding, M.; Shang, Y.; Chen, S. Promoting Highly Reversible Sodium Storage of Iron Sulfide Hollow Polyhedrons *Via* Cobalt Incorporation and Graphene Wrapping. *Adv. Energy Mater.* **2019**, *9*, 1901584.
(26) Yang, D.; Chen, W.; Zhang, X.; Mi, L.; Liu, C.; Chen, L.; Guan, X.; Cao, Y.; Shen, C. Facile and Scalable Synthesis of Low-Cost FeS@C as Long-Cycle Anodes for Sodium-Ion Batteries. *J. Mater. Chem. A* **2019,** *7*, 19709-19718.
(27) Jin, A.; Kim, M.-J.; Lee, K.-S.; Yu, S.-H.; Sung, Y.-E. Spindle-Like Fe_7S_8/N-Doped Carbon Nanohybrids for High-Performance Sodium Ion Battery Anodes. *Nano Research* **2019,** *12*, 695-700.
(28) Wang, H.; Qian, X.; Wu, H.; Zhang, R.; Wu, R. Mof-Derived Rod-Like Composites Consisting of Iron Sulfides Embedded in Nitrogen-Rich Carbon as High-Performance Lithium-Ion Battery Anodes. *Appl. Surf. Sci.* **2019,** *481*, 33-39.
(29) Liu, Y.; Zhang, L.; Liu, D.; Hu, W.; Yan, X.; Yu, C.; Zeng, H.; Shen, T. Turbostratic Carbon-Localised FeS_2 Nanocrystals as Anodes for High-Performance Sodium-Ion Batteries. *Nanoscale* **2019,** *11*, 15497-15507.
(30) Pan, Q.; Zheng, F.; Liu, Y.; Li, Y.; Zhong, W.; Chen, G.; Hu, J.; Yang, C.; Liu, M. $Fe_{1-x}S$@S-Doped Carbon Core-Shell Heterostructured Hollow Spheres as Highly Reversible Anode Materials for Sodium Ion Batteries. *J. Mater. Chem. A* **2019,** *7*, 20229-20238.
(31) Chen, K.; Li, G.; Wang, Y.; Chen, W.; Mi, L. High Loading FeS_2 Nanoparticles Anchored on Biomass-Derived Carbon Tube as Low Cost and Long Cycle Anode for Sodium-Ion Batteries. *Green Energy & Environment* **2019**. DOI:10.1016/j.gee.2019.11.001.
(32) Ma, J. M.; Lian, J. B.; Duan, X. C.; Liu, X. D.; Zheng, W. J. Alpha-Fe_2O_3: Hydrothermal Synthesis, Magnetic and Electrochemical Properties. *J. Phys. Chem. C* **2010,** *114*, 10671-10676.
(33) Malard, L. M.; Pimenta, M. A.; Dresselhaus, G.; Dresselhaus, M. S. Raman Spectroscopy in Graphene. *Phys. Rep.* **2009,** *473*, 51-87.
(34) Wu, H. L.; Huff, L. A.; Gewirth, A. A. In Situ Raman Spectroscopy of Sulfur Speciation in Lithium-Sulfur Batteries. *ACS Appl. Mater. Interfaces* **2015,** *7*, 1709-1719.
(35) Zhang, P.; Zhao, X.; Liu, Z.; Wang, F.; Huang, Y.; Li, H.; Li, Y.; Wang, J.; Su, Z.; Wei, G. Exposed High-Energy Facets in Ultradispersed Sub-10 nm SnO_2 Nanocrystals Anchored on Graphene for Pseudocapacitive Sodium Storage and High-Performance Quasi-Solid-State Sodium-Ion Capacitors. *NPG Asia Mater.* **2018**, *10*, 429-440.
(36) Liu, Z.; Hu, F.; Xiang, J.; Yue, C.; Lee, D.; Song, T. A Nano-Micro Hybrid Structure Composed of Fe_7S_8 Nanoparticles Embedded in Nitrogen-Doped Porous Carbon Framework for High-Performance Lithium/Sodium-Ion Batteries. *Part. Part. Syst. Char.* **2018,** *35*, 1800163.
(37) He, Q. M.; Rui, K.; Yang, J. H.; Wen, Z. Y. Fe_7S_8 Nanoparticles Anchored on Nitrogen-Doped Graphene Nanosheets as Anode Materials for High-Performance Sodium-Ion Batteries. *ACS Appl. Mater. Interfaces* **2018,** *10*, 29476-29485.
(38) Xiong, P. X.; Zhao, X. X.; Xu, Y. H. Nitrogen-Doped Carbon Nanotubes Derived from Metal-Organic Frameworks for Potassium-Ion Battery Anodes. *Chemsuschem*

2018, *11*, 202-208.
(39) Hou, B. H.; Wang, Y. Y.; Guo, J. Z.; Zhang, Y.; Ning, Q. L.; Yang, Y.; Li, W. H.; Zhang, J. P.; Wang, X. L.; Wu, X. L. A Scalable Strategy to Develop Advanced Anode for Sodium-Ion Batteries: Commercial Fe_3O_4-Derived Fe_3O_4@FeS with Superior Full-Cell Performance. *ACS Appl. Mater. Interfaces* **2018,** *10*, 3581-3589.
(40) Yang, H.; Xu, R.; Yao, Y.; Ye, S. F.; Zhou, X. F.; Yu, Y. Multicore-Shell Bi@N-Doped Carbon Nanospheres for High Power Density and Long Cycle Life Sodium- and Potassium-Ion Anodes. *Adv. Funct. Mater.* **2019,** *29*, 1809195.